Earth and Space Science

RESEARCH ARTICLE
10.1029/2019EA001036

Key Points:
- An algorithm is developed to integrate GPS and InSAR data for 3D crustal deformation field.
- GPS data are optimally interpolated, and GPS and InSAR data are weighted with realistically estimated uncertainties.
- Method application to real data reveals water withdrawal induced subsidence and drought caused uplift at regions in southern California.

Supporting Information:
- Supporting Information S1

Correspondence to:
Z.-K. Shen,
zshen@ucla.edu

Citation:
Shen, Z.-K., & Liu, Z. (2020). Integration of GPS and InSAR data for resolving 3-dimensional crustal deformation. *Earth and Space Science*, *7*, e2019EA001036. https://doi.org/10.1029/2019EA001036

Received 6 DEC 2019
Accepted 14 MAR 2020
Accepted article online 20 MAR 2020

Integration of GPS and InSAR Data for Resolving 3-Dimensional Crustal Deformation

Zheng-Kang Shen[1] and Zhen Liu[2]

[1]Department of Earth, Planetary and Space Sciences, University of California, Los Angeles, CA, United State, [2]Jet Propulsion Laboratory, California Institute of Technology, Pasadena, CA, United State

Abstract We develop an algorithm to integrate GPS and InSAR data for a 3-dimensional crustal deformation field at the Earth's surface. In the algorithm discrete GPS data points are interpolated to obtain a 3-dimensional continuous velocity field, which is then combined with the InSAR line-of-sight (LOS) velocity data pixel by pixel using the least-squares method. Advantages of our method over previous ones are that: 1) The GPS data points are optimally interpolated by balancing a trade-off between spatial resolution and solution stability. 2) A new algorithm is developed to estimate realistic uncertainties for the interpolated GPS velocities, to be used as weights for GPS data in GPS-InSAR combination. 3) Realistic uncertainties for the InSAR LOS rate data are estimated and used as weights for InSAR data in GPS-InSAR combination. 4) The ramps and/or offsets of the InSAR data are globally estimated for all the images to minimize data misfit, particularly at regions where the data overlaps. Application of this method to real data from southern California shows its capability of successfully restoring 3-dimensional continuous deformation field from spatially limited GPS and dimensionally limited InSAR data. The deformation field reveals water withdrawal induced subsidence and drought caused uplift at various regions in southern California.

1. Introduction

The Global Positioning System (GPS) and the Interferometric Synthetic Aperture Radar (InSAR) are two satellite geodesy methods that have been widely used in recent years to measure crustal deformation. The GPS method can be used to precisely measure 3-dimensional positions and displacements at discrete locations, with up to one millimeter accuracy in horizontal directions and several millimeters accuracy in vertical direction (Bock & Melgar, 2016). The InSAR techniques can be used to measure areal displacements in the direction of radar line-of-sight (LOS) up to several millimeters to centimeter accuracy (Gens and Van Genderen, 1996). These two methods are therefore complementary to each other for crustal deformation monitoring, and efforts have been made to combine these two kinds of observations with common spatial and temporal span, for better spatial and temporal resolution than using either one of them. Such kinds of efforts include: 1) Construct a 3-dimential velocity field using a GPS derived velocity model to control the long-wavelength deformation and InSAR data to constrain the short-wavelength deformation (e.g. Tong et al., 2013). 2) Interpolate 3-dimensional GPS velocity and combine that with the InSAR LOS rate data by point-by-point least-squares regression (e.g. Samsonov et al., 2007, 2008). 3) Integrate 3-dimensional GPS time series at discrete locations with 1-dimensional InSAR LOS time series data for 3-dimensional continuous time series (e.g. Gudmundsson et al., 2002). In this study we focus on the approach 2), and develop an algorithm to optimally integrate GPS and InSAR data sets for the production of 3-dimensional crustal velocity solution. We will also demonstrate the usefulness of the algorithm with a case study at a selected region in southern California. This method can be extended further to the combination of GPS and InSAR time series data. The code to perform the combination is released to interested users as a supporting information dataset to this paper.

2. Methodology

2.1. GPS Data Interpolation and Uncertainty Estimation

GPS station velocities can be derived from position time series of either campaign or continuous GPS observations. In this study as an example, we use velocity solutions of continuous GPS (CGPS) sites produced by

10.1029/2019EA001036

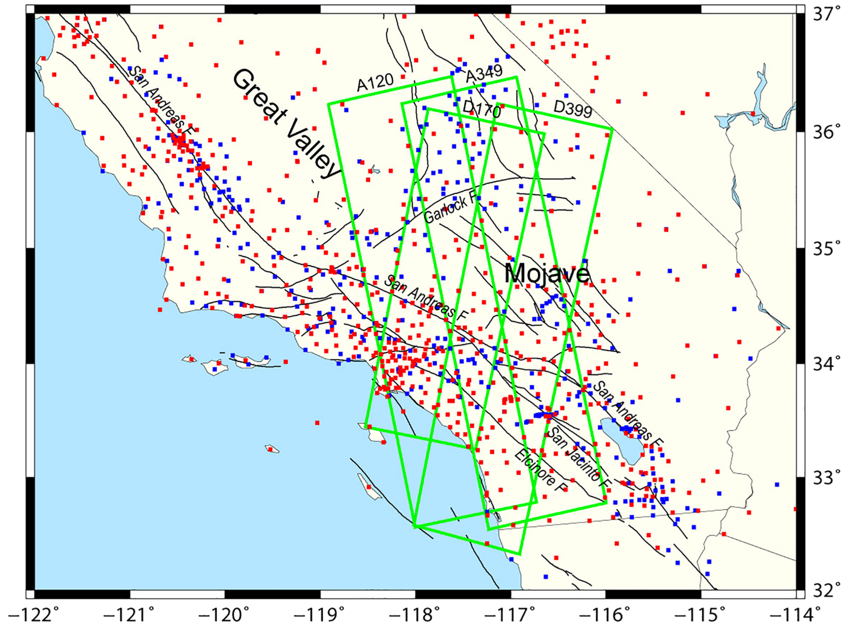

Figure 1. Study area in southern California. Black curves are active faults, red and blue squares are GPS sites whose 3D and 2D (horizontal only) data are used in this study respectively. The green frames denote the imprints of 4 InSAR tracks whose data are used in this study.

the MEaSUREs project (ftp://sopac-ftp.ucsd.edu/pub/timeseries/measures/ats/), and of campaign GPS sites from the SCEC Crustal Motion Map version 4 (CMM4) solution (Shen et al., 2011) (Figures 1 and 2). The CMM4 velocities are rotated to align with the CGPS solution which is referenced to the stable North America reference frame (SNARF) (Herring et al., 2008). We divide the GPS data into two groups. The first group utilizes the 3-l dimensional velocity components for solution, which includes most of the CGPS sites from the MEaSUREs project. The second group utilizes only the horizontal velocity components, which includes the CMM4 sites and a small portion of the CGPS sites whose vertical velocities show anomalously large and possibly non-tectonic signals. Both data sets are screened to remove outliers, and 1052 horizontal and 542 vertical site velocities are employed. Separate interpolations are performed for the horizontal and vertical velocity fields, to account for different data populations.

GPS data uncertainties are used to weight the data input in interpolation, and are examined for their adequacy. Uncertainties for the CGPS velocities were derived from the time series analysis of the sites, and are mostly around 0.1–0.2 mm/yr for the horizontal components. These uncertainty estimates, however, may reflect only the intrinsic errors of the data time series, and not the epistemic errors associated with the sites. Such epistemic errors may arise for example from long-term hydraulic circulation beneath the site monument, and/or slow aging of the electronic device of the receiver instruments. A calibration is therefore needed for the GPS velocity uncertainties. We use GPS velocity data from closely located station pairs to determine the lower cutoff threshold of the velocity uncertainties. For a pair of closely located GPS sites, the tectonic motion velocities should be practically the same if the sites are located in a region with no or slow tectonic deformation. We thus perform statistical analysis for differential velocities of such station pairs, and obtain the median values of 0.6, 0.6, and 1.0 mm/yr for the east, north, and up components from 25 station pairs in our dataset, whose relative distances are less than 0.2 km. We therefore set 0.6 and 1.0 mm/yr as the lower cutoff uncertainties for the horizontal and vertical velocity components, respectively.

In our algorithm of GPS and InSAR data integration, point-based discrete GPS velocities are first interpolated to produce continuous 3-D vector map at chosen grids. The interpolation is based on an algorithm of Shen et al. (2015), which takes into account GPS network density and configuration for data weighting. A Gaussian distance weighting function (w_d) and a Voronoi cell spatial weighting function (w_v) are used in the interpolation, which allow greater weighting for sites located closer to the chosen grid and/or occupying greater Voronoi cell areal space. The amount of weighting and degree of smoothing can be spatially variable

10.1029/2019EA001036

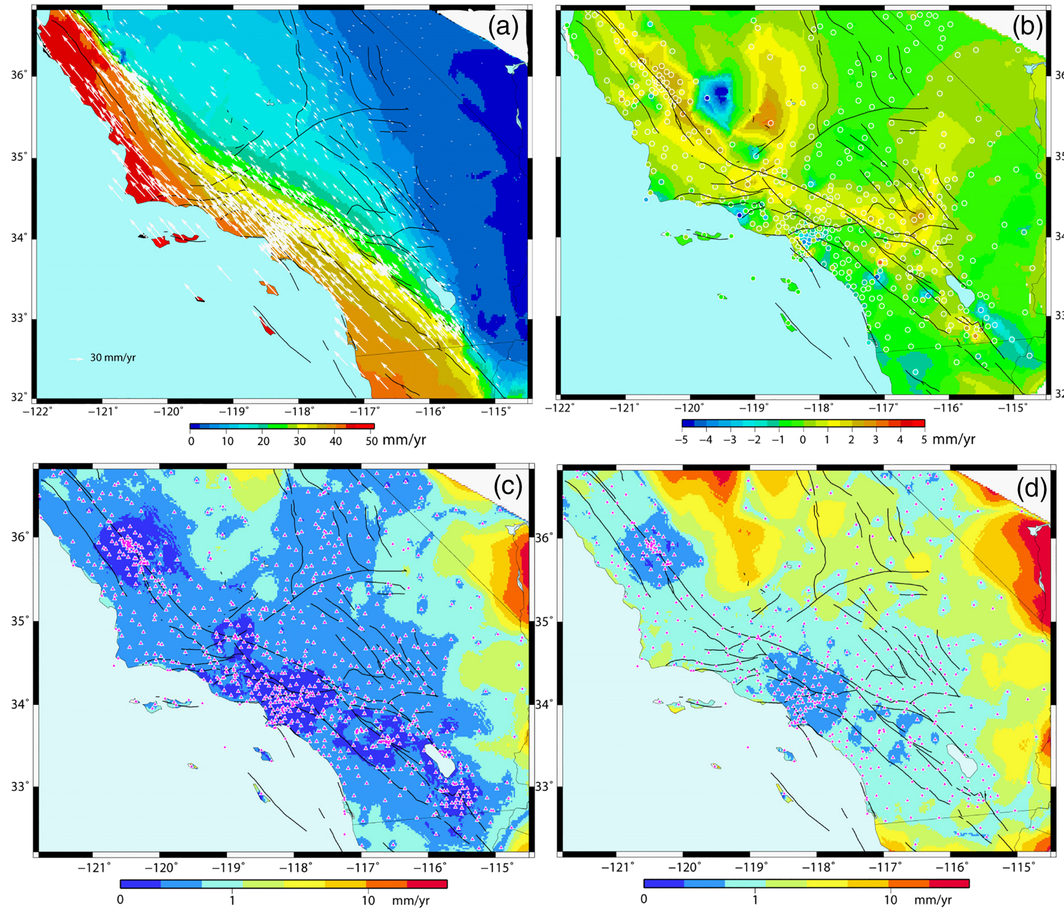

Figure 2. GPS velocities and interpolation result. (a) White vectors are GPS horizontal velocities in SNARF reference frame that are used in the combination with InSAR data. The background colors denote the amplitudes of interpolated horizontal velocity field. (b) Filled circles are GPS vertical observations, and the background colors denote the interpolated vertical velocity field. (c) and (d) are uncertainties of east and up components of interpolated GPS velocities, respectively. Magenta triangles denote the locations of GPS sites.

and optimally determined based on *in situ* data strength, and are realized by assigning a common weighting parameter W for all the grid points: $W = \sum_{i=1}^{n\_k} w_d^i(k)^* \mathrm{w}_v^i(k)$. n_k is the number of neighboring data points used for the k^{th} grid point, $w_d^i(k) = \exp\left(-\frac{r_i^2}{\sigma_k^2}\right)$ is the Gaussian distance weighting function, r_i is the distance between the i-th GPS site and the grid point, and σ_k is the smoothing distance constant. At each grid point σ_k is adjusted to meet W, which is a predetermined constant. With this adjustment, less smoothing is performed and better resolution is achieved for grids with denser data coverage, and vice versa. This approach can also effectively smooth out the incoherencies in discretized GPS velocity data and produce robust joint inversion result. Selection of the parameter W allows an overall control of the degree of smoothing for the solution. Greater W would result in more sites included for interpolation and more smoothed solution with less resolution, and smaller W would result in less sites included and less smoothed solution with better resolution. An optimal balance can be achieved by assessing the overall data strength of the network. Figure S1 shows spatial distribution of σ_k. It demonstrates different degree of smoothing in southern California based on the network densities in the region.

To combine the interpolated GPS data with InSAR data, we need adequate estimates of GPS velocity uncertainties from the interpolation, to be used as data weighting in the combination. Formal GPS velocity uncertainties deduced in the interpolation process, however, are not fit for the job because they are largely determined by the amount of a priori information (i.e. the degree of smoothing) imposed during interpolation, which varies from grid to grid. It usually leads to apparently unreasonable results, that regions with

Table 1
SAR acquisitions and interferograms used in the study

Track	Heading	Sensors	Time span	Dates # of looks	Interferogram pairs
170	descending	ERS + Envisat	1992/06/17–2010/09/25	D170_ers_dates.list 71 D170_env_dates.list 51	D170_ers_pairs.list D170_env_pairs.list
399	descending	Envisat	2003/06/30–2010/05/24	D399_dates.list 49	D399_pairs.list
349	ascending	Envisat	2003/11/14–2010/10/08	A349_dates.list 49	A349_pairs.list
120	ascending	Envisat	2003/10/29–2010/09/22	A120_dates.list 53	A120_pairs.list

sparser data points would have smaller uncertainty than regions with denser data points, and vice versa. To overcome the problem, we propose to propagate errors from GPS data input to interpolation output using the same interpolation functional form and least-square procedure as before, but not to alter the smoothing distance parameter σ_k. Instead, σ_k will be kept as a constant σ_0 for all the region. In this way the same kind of a priori assignment algorithm will be applied for all the grids, and the only difference reflected in the output uncertainty estimates will be the in situ data strength; the denser the local observation network is, the smaller the uncertainty will be, and vice versa. Parameter σ_0 is then determined through a statistical bootstrapping procedure. In the procedure velocity interpolation is performed at each GPS site without utilization of the velocity datum of the site, and a differential velocity is evaluated for the site between the datum of the site and the interpolation value. We perform the bootstrapping analysis iteratively for all the sites with different assumptions of σ_0, and the optimal value of σ_0 (=17 km) is determined when the median of the amplitudes of 3-dimensional residual velocities at the GPS sites is equal to the median of the uncertainties from GPS site velocity interpolation. Figure S2 plots histograms of the interpolated GPS site velocity uncertainties and the bootstrapping velocity residuals with the optimal value of σ_0 incorporated, and the result shows an overall consistency of the two series.

2.2. InSAR Data Processing, LOS Rate and Uncertainty Estimation

Here we briefly describe InSAR processing and analysis steps for the InSAR data used in the case study for southern California. We processed the raw SAR data of ERS-1,2 and Envisat satellites from 1992 to 2010 for interferograms using a modified version of JPL/Caltech ROI_PAC software package. Major processing steps include interferometric phase flattening using precise orbit, topography phase correction based on 2-arc SRTM digital elevation model (DEM), baseline re-estimation for orbital error correction when needed, phase unwrapping, filtering and geocoding. For the ERS-2 data after 2001 that have Doppler issue due to gyroscope failure, we employ a maximum entropy approach to resolve Doppler ambiguity and identify all usable ERS-2 interferometric pairs. For Envisat ASAR sensors, we correct temporally correlated range ramp error due to long-term local oscillator frequency drift by adopting an empirical approach (Marinkovic & Larsen, 2013). Comparison with in-situ GPS shows that such a correction works well and reduces the RMS error between InSAR and GPS velocities to less than 2 mm/yr (Liu et al., 2014).

We use a variant of the Small Baseline Subset InSAR time series approach to solve for InSAR LOS time series and mean velocity (e.g., Sansosti et al., 2010). We incorporate topography dependent troposphere delay correction, residual DEM error and earthquake offset estimate, and employ spatiotemporal filtering to remove high frequency turbulent troposphere noise (Liu et al., 2014; Samsonov, 2010). Since orbital ramp error for data from the same track is typically limited to a few acquisitions (e.g., Fattahi & Amelung, 2014) and small, we correct only affected interferograms through baseline re-estimation with the constraint of a priori GPS based deformation model. The number of pairs with such correction is much less than the total number of interferograms that went into the analysis. This ensures that the influence of a priori model is negligible. Hundreds of interferograms that meet spatial and temporal baseline criteria are formed and used in the time series inversion. Table 1 lists SAR data acquisition and interferograms used in the study. More information about the dates of satellite data and the satellite image pairs for the interferograms is listed in Tables S1 and S2, respectively.

The InSAR data are weighted by their LOS uncertainties. To characterize the uncertainties associated with InSAR deformation map, we adopt a Jackknife variance estimation approach (Efron & Stein, 1981), which

10.1029/2019EA001036

provides a reasonable way to account for uncertainties arisen from lacking or missing dates, uncorrected residuals or other noises, and/or the influence of reference pixel and date.

2.3. GPS and InSAR Velocity Data Combination

We combine GPS interpolated velocities and InSAR LOS rate data to produce a spatially continuous 3-dimensional velocity field. We first divide the region into rectangle grid cells. At each grid cell, all of the available InSAR LOS rate data from different tracks (with different viewing geometries) are used. For each of the LOS rate images all the pixel data within the grid cell are averaged to produce a mean rate, weighted by the uncertainties. The binned averages are also made for azimuth angle, look direction, and LOS uncertainty (which is averaged the same way as the other observables) associated with the LOS measurements. The binned LOS data are then compared with GPS data to determine the scale factors for LOS uncertainties. For each selected track of data we compute the differences between the LOS data input and the LOS values projected from GPS velocities at grid cells with GPS occupation. We then determine a scaling factor which is the ratio of two median values: one is for the differences in LOS data and another is for the averaged LOS uncertainties (Figure S3). The scaling factor is used to scale the data uncertainties accordingly. The InSAR data and rescaled uncertainties are used as data inputs for subsequent analysis.

Because of relative measurements and selections of different reference regions, the InSAR LOS velocities usually have offsets between different tracks. The residual orbital error and/or remaining atmospheric phase noise that are not fully corrected may also introduce subtle ramp difference between tracks. The first step in GPS/InSAR combination is therefore to solve for the offsets/ramps of InSAR images. Since InSAR data provide only LOS measurements from ascending and/or descending viewing geometry, the offset/ramp parameters have to be solved together with the 3-dimensional deformation components, and some GPS data and their interpolated values are needed in the estimate to stabilize the inversion. Because these offset/ramp parameters are correlated with all the deformation parameters in the study area, an optimal estimate of the offsets/ramps means a global solution for all the parameters involved. However, the number of parameters for the 3-dimensional velocity field can be huge, up to millions or even billions depending on the scope of the study area and the size of the grid cells provided, thus it may not be practical and/or even necessary to solve for all the parameters in a single least-squares solution. We therefore include GPS data at only a limited number of grid points in the solution in this step. Two groups of grid points are accounted: the first group includes all the grid points containing direct GPS velocity observations, and the second group involves decimated grid points with multiple InSAR data entries. Incorporation of the data in the second category helps reinforce the solution for the offsets/ramps, but only at decimated grid points (e.g. by a factor of 10 in each dimension in the overlapped regions) would be sufficient for the purpose. The problem is thus formulated as:

$$\begin{pmatrix} V \\ S \end{pmatrix} = \begin{pmatrix} I & 0 \\ P & K \end{pmatrix} \begin{pmatrix} U \\ R \end{pmatrix} + \begin{pmatrix} \varepsilon_v \\ \varepsilon_s \end{pmatrix} \tag{1}$$

where $V^{\mathrm{T}} = (V_1, V_2, \dots V_N)$, and $V_i = (V_e, V_n, V_u)_i^{\mathrm{T}}$ is the interpolated GPS velocity vector at the i-th site. $S^{\mathrm{T}} = (S_1, S_2 \dots S_m)^{\mathrm{T}}$ is the InSAR LOS data for the site. $U^T = (U_1, U_2, \dots U_N)^T$, and $U_i = \begin{pmatrix} U_e \\ U_n \\ U_u \end{pmatrix}_i$ is the velocity vector to be solved. $R = \begin{pmatrix} R_1 \\ \dots \\ R_m \end{pmatrix}$ is the array for all the satellite offset and ramp error correction terms, and $R_i = \begin{pmatrix} R_0^i \\ R_e^i \\ R_n^i \end{pmatrix}$ is the array for offset and ramp error correction of the i-th satellite, with the three components as for the offset (R_0) and the east and north ramps (R_e, R_n), respectively. $P = \begin{pmatrix} p_1 \\ \vdots \\ p_n \end{pmatrix}$, in which $p_i = (p_e, p_n, p_u)_{\mathrm{i}}$ is a unit vector to project the velocity vector into the LOS of the i-th satellite. $K =$

$\begin{pmatrix} k_1 & \cdots & 0 \\ \vdots & \ddots & \vdots \\ 0 & \cdots & k_m \end{pmatrix}$ is the array for partial derivatives of the ramp correction terms, $k_i = (1, r_e, r_n)_{\mathrm{i}}$ is for the i-th satellite, and r_e and r_n are partial derivatives for the east and north ramp components respectively. ε_v and ε_s are error arrays for GPS and InSAR data respectively, ε_v ~N(0, C_v) and ε_s ~N(0, C_s); C_v and C_s are the error covariance matrices, whose diagonal terms are the squares of the estimated GPS and InSAR data uncertainties respectively. Let the equation be rewritten as:

$$y = Ax + \varepsilon \tag{2}$$

its least-squares solution is $x = (A^{\mathrm{T}}C^{-1}A)^{-1}A^{\mathrm{T}}C^{-1}y$.

In the second step the components of offsets/ramps are removed from the InSAR LOS data, and the 3-dimensional velocity is solved for each grid cell through least-squares regression, with GPS interpolated velocity and LOS data for the cell incorporated. The adaptive and rescaled GPS and InSAR data uncertainties are used to weight the data input. The GPS vertical data may or may not be used to constrain the final solution, depending on the quality and reliability of the data.

3. GPS-InSAR Combination in Southern California

3.1. GPS-InSAR Data Combination

We apply the GPS-InSAR combination method to a region in southern California covered by 4 ground tracks of ERS and Envisat satellites (Figure 1). The InSAR data delineate an area of approximately 32.5°-36°N, 116°-118.5°W, covering the southern part of the Eastern California Shear Zone, the Mojave Desert, the central Transverse Ranges, and the coastal area from Los Angeles to San Diego. Active faults in the region include the Mojave and San Bernardino segments of the San Andreas, Garlock, Mojave Shear Zone, Owens Valley, San Jacinto, and Elsinore faults.

The GPS velocity dataset used in the study is shown in Figure 2, along with the interpolated velocities and their uncertainties. As described in the previous section, we adopt an algorithm to determine uncertainties of the interpolated velocities, which employs the same degree of smoothing for all the grid cells, and considers GPS network distribution and site-specific uncertainties to determine uncertainties of the velocity solution. The data weighting threshold W for southern California is set to be 3, and the optimal smoothing constant σ_0 for uncertainty evaluation is 17 km, determined by scaling analysis.

Four tracks of InSAR data sets are used in the study (Figure 3). The data are the LOS velocities from our previous InSAR time series analysis (Liu et al., 2014), including the following: (a) descending track 170 derived from ERS/Envisat data over the period of 1992–2010; (b) descending track 399 from Envisat over the period of 2003–2010; (c) ascending track 349 from Envisat over the period of 2003–2010; and (d) ascending track 120 from Envisat over the period of 2003–2010. The lower panel of Figure 3 shows the estimated uncertainties for the LOS velocity data after rescaling, with the scaling factors of 4.58, 1.26, 4.87, and 1.53 for tracks of 170, 120, 349, and 399, respectively. The result shows that although uncertainties are relatively uniform for track 170, they vary considerably for tracks 399, 349, and 120. For tracks 399, 349, and 120, we only use Envisat data for interseismic velocity estimates as these tracks spanning the East California Shear Zone (ECSZ). The ERS data from these tracks are not used because they are likely affected by postseismic deformation following the 1992 Landers and 1999 Hector Mines earthquakes in the ECSZ area. This resulted in fewer SAR images for tracks 399, 349, and 120 than for track 170, and among which a few images were affected significantly by atmospheric disturbance with strong spatial variations. This is particularly true for track 349, with the residual atmosphere noise resulting in the largest errors for the northern and southern parts of the track where the LOS rate uncertainties are up to 5 mm/yr.

A suite of combination models are tested with various selection of model parameters, including the choices of InSAR data uncertainties, the use of GPS vertical data for model constraints, and the InSAR offset/ramp estimation, etc. Table 2 lists parameter setups of four models tested and the modeling statistics.

Figure 4 shows the result of model A, which has 3 common parameters solved for each InSAR image, namely the constant offset and the east and north trends for the ramp. The estimated LOS uncertainties are used to

10.1029/2019EA001036

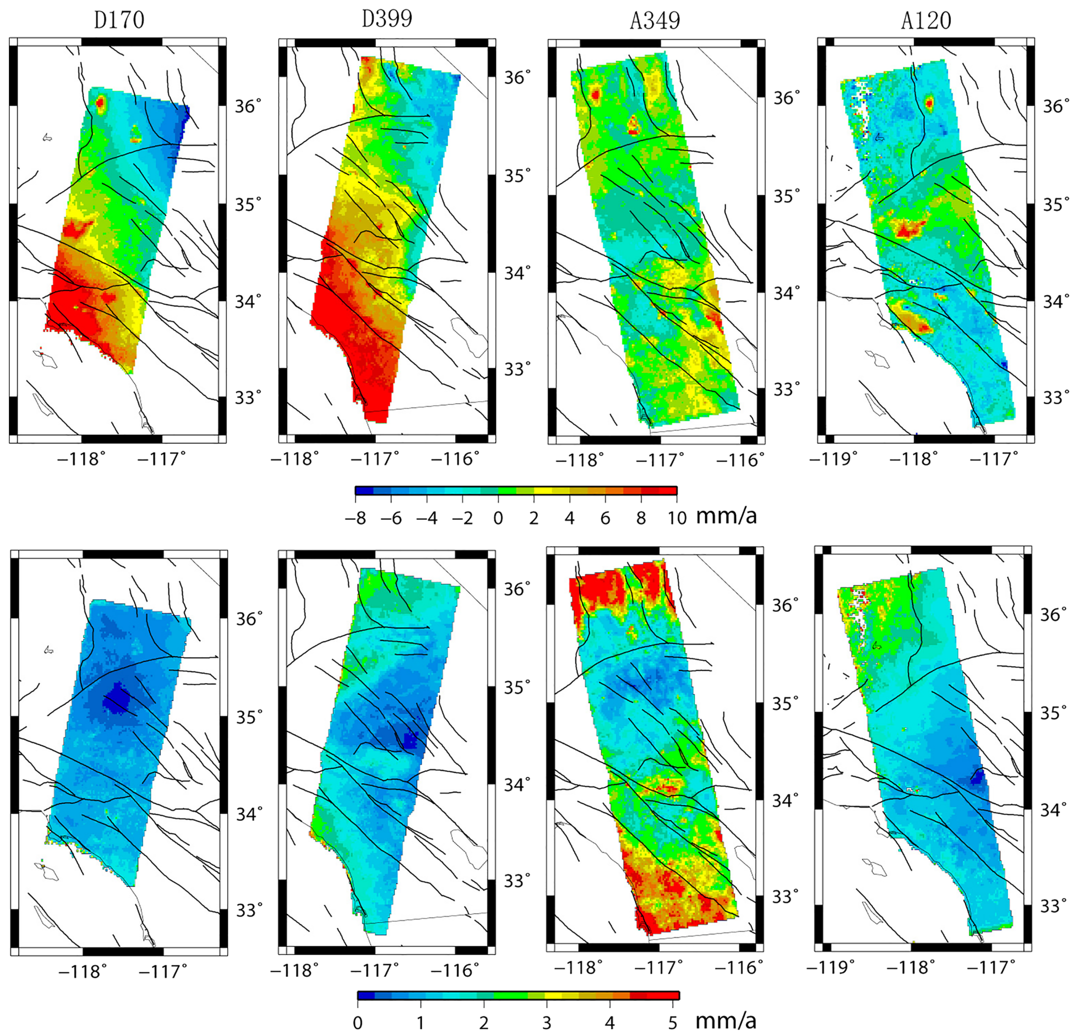

Figure 3. InSAR LOS data from 4 selected tracks of D170, D399, A349, and A120 that are used in the combination. The upper panel shows the LOS velocities, and the lower panel shows the corresponding uncertainties, respectively.

weight the data, with a lower cut-off threshold of 1 mm/yr. This ad hoc cut-off threshold is set to account for the effects of residual atmospheric noise or other unmodeled noise. The GPS vertical data are used in derivation of the ramps of the InSAR data but not the final solution of the vertical velocities. The InSAR data postfit residuals and the model formal uncertainties are demonstrated in Figure 5. Only the

Table 2
Combination model results

Model #	InSAR-σ	GPS vertical	Ramp/offset	χ^2_w	χ^2_w/n	χ^2_{uw}	χ^2_{uw}/n
A	Estimated	Not used	Ramp	$1.36\text{x}10^4$	0.34	$4.30\text{x}10^4$	1.07
B	Default	Not used	Ramp	$0.89\text{x}10^4$	0.22	$3.56\text{x}10^4$	0.89
C	Estimated	Used	Ramp	$2.64\text{x}10^4$	0.66	$7.21\text{x}10^4$	1.80
D	Estimated	Not used	Offset	$2.59\text{x}10^4$	0.65	$7.66\text{x}10^4$	1.91

χ_{w}^2: Total weighted postfit residual χ^2.
χ_{w}^2/n: Reduced weighted postfit residual χ^2.
χ_{uw}^2: Total unweighted postfit residual χ^2.
χ_{uw}^2/n: Reduced unweighted postfit residual χ^2.

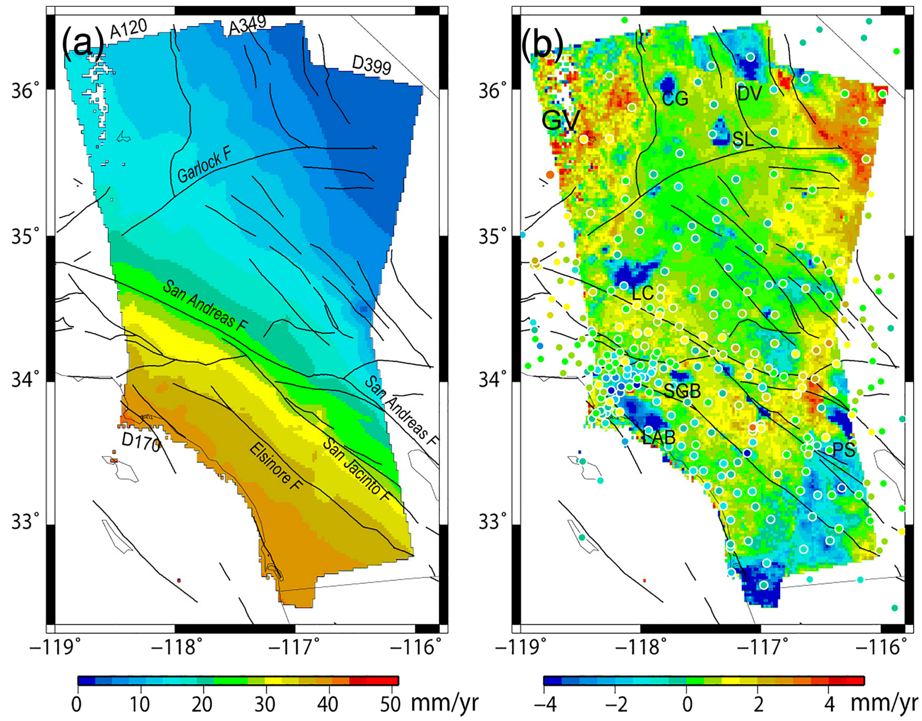

Figure 4. Combined GPS and InSAR 3-D velocities for model A, with estimated InSAR data uncertainties to weight the data and SAR satellite orbital ramps estimated. (a) shows amplitudes of the horizontal components, and (b) the vertical components, respectively. Round dots in (b) are GPS vertical velocities, which are used in the orbital ramp estimation but not the 3-D velocity solution. Name abbreviations: CG, Coso Geotherm site; DV, Death Valley; GV, Great Valley; LAB, Los Angeles Basin; LC, Lancaster; PS, Palm Springs; SB, San Gabriel Basin; SL, Searles Lake.

uncertainties of the east and vertical components are shown. Uncertainties of the north component are not shown which are very similar to that of the east component.

We test three other models with different parameterizations. Model B is similar to Model A except that instead of estimated uncertainties for InSAR data, a default LOS uncertainty of 2 mm/yr is adopted to constrain the solution. The 3-dimensional velocity solution is shown in Figure S4, and the InSAR data postfit residuals and the model formal uncertainties are demonstrated in Figure S5. Model C tests the use of GPS vertical data to constrain the final solution, and the solution is shown in Figure 6 and the postfit residuals and solution uncertainties are displayed in Figure 7, respectively. Model D tests the sensitivity estimation of the ramp parameters to the solution, and the result is shown in Figures S6 and S7.

3.2. GPS and InSAR Contribution to Solution

We apply our GPS-InSAR combination method to southern California, which has arguably the best GPS and InSAR data coverage in the world to monitor crustal deformation. As a result, our horizontal velocity field is solved at the precision of ~0.7 mm/yr for most of the studied area, and the vertical velocity field is determined with <1.5 mm/yr uncertainty for most of the region with multiple LOS data coverage, and < 2.5 mm/yr for the region with one LOS data entry (Figure 5). Our method works well to resolve the 3-dimensional deformation field in the region. However, how would the method perform for a region with less dense data coverage? Particularly, if the GPS network is not so dense, how would the deformation field be resolved? How would GPS and InSAR each contribute, for both the horizontal and vertical solutions? To prove a concept, we perform tests for two sample cases with less GPS data input to assess how the solutions would be impacted, and address the questions raised above.

In the first test case we incorporate GPS velocity data from a CGPS network of 300 sites. These sites are sampled from our original CGPS network in an iterative procedure, each time removing one site which has the closest distance to others. The sites retained at last are with relatively evenly distributed spacing.

10.1029/2019EA001036

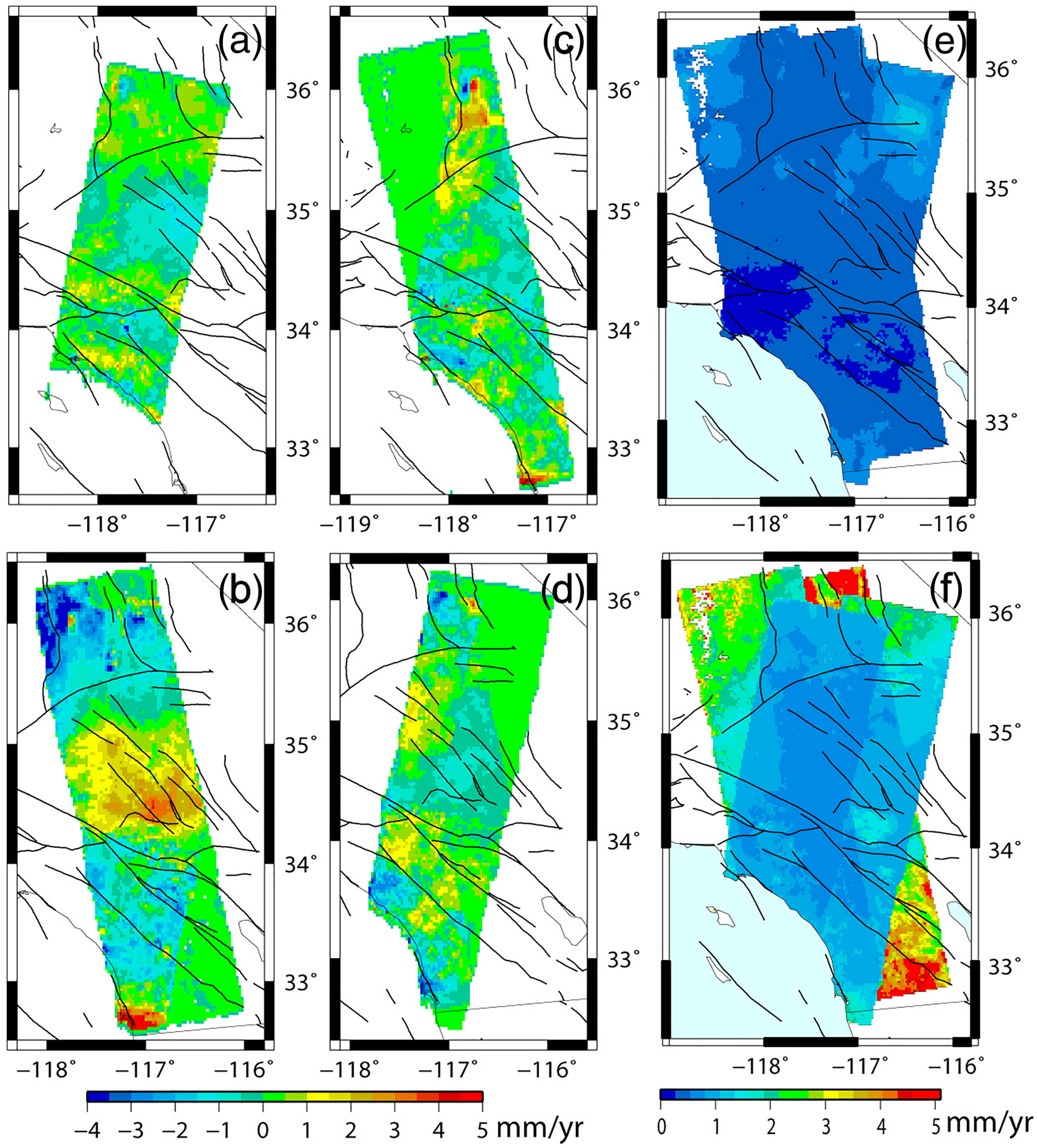

Figure 5. Data postfit residuals and solution uncertainties for model A. (a), (b), (c) and (d) are InSAR LOS postfit residuals for tracks D170, A349, A120, and D399, respectively. (e) and (f) are solution uncertainties for the east and vertical components respectively.

Figure S8 shows the spatial distributions of the sites and the smoothing distance σ_k. Because of the sparser station distribution, the smoothing distance σ_0 used for the GPS uncertainty estimate is evaluated as 28 km, determined from the scaling analysis. Figure S2b shows the histogram of the data used in the analysis. This GPS velocity dataset is then combined with the same InSAR dataset to deduce the 3-dimensional velocity solution (named as Model T1). Figure 8 shows the velocity solution, and Figure S9 the residual velocities between GPS interpolated velocities and the combined solution velocities. The result shows significant residual velocities for the vertical component, which is expected as vertical GPS data are not used in the combined solution. The residual velocities for the horizontal component, however, are very small (< 0.1 mm/yr) for most of the region, except for a small patch in the Coso area with up to 1 mm/yr velocity difference. This result suggests that for a GPS network of ~30 km spacing, the GPS data are capable of providing overwhelming constraints for the solution of continuous horizontal deformation, and contributions from InSAR are mostly insignificant. Exceptions could occur at places with localized

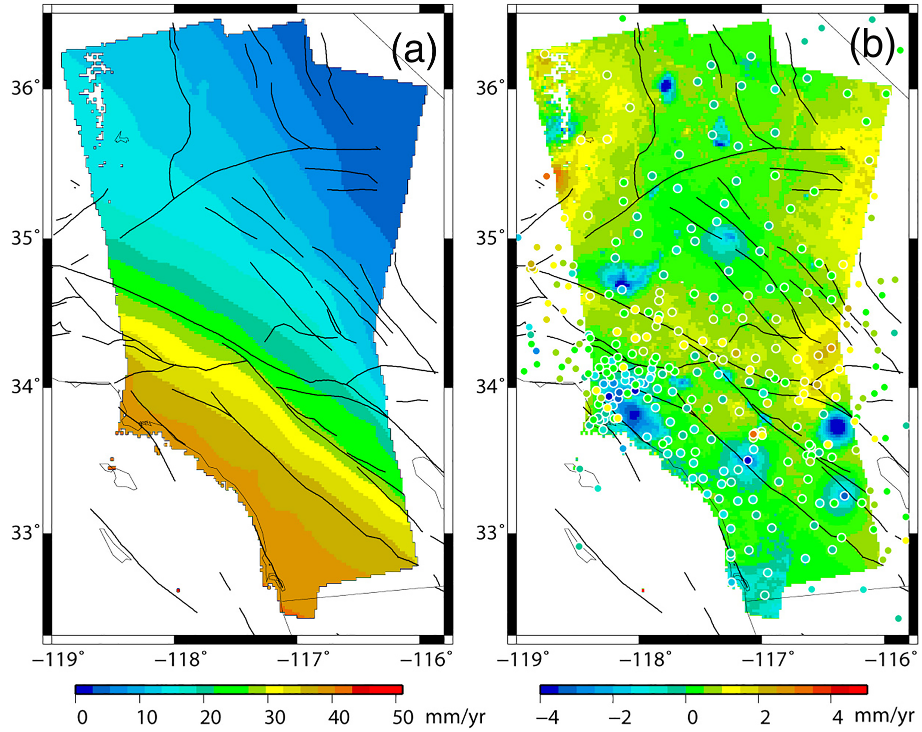

Figure 6. Combined GPS and InSAR 3-dimensional velocities for model C, with estimated InSAR data uncertainties to weight the data and SAR satellite orbital ramps estimated. (a) shows amplitudes of the horizontal components, and (b) the vertical components, respectively. Round dots in (b) are GPS vertical velocities, which are used in both estimation of orbital ramps and the final 3-dimensional velocity solution.

deformation sources, e.g. creeping in central and southern San Andreas fault and geothermal activity in the Coso area, as mentioned above.

Figure S10 shows uncertainties for the combined solution. Comparing to the solution uncertainties of Model A (Figure 5), we find that uncertainties for the vertical component have not changed much, because they are mainly constrained by the InSAR data and the InSAR data input for Model T1 are the same as that used in Model A. Uncertainties for the horizontal components, however, have some significant changes, particularly for that around the Los Angeles basin area where very dense GPS data are used in Model A but not in Model T1. The horizontal uncertainties in the Los Angeles basin area for Model T1 are ~0.6 mm/yr, comparing to that of ~0.3 mm/yr for Model A. We also plot the differential velocities between the Model A and Model T1 solutions, and the result is shown in Figure 9. As can be seen, most of the noticeable differences are located around active fault zones, which is due to the reduction of spatial resolution of GPS interpolated velocity field, that without a dense network some subtle velocity gradients in these fault zones would be missed in the solution of Model T1. The velocity residuals range 0.5–1.5 mm/yr for most of the region, which is consistent with the uncertainty estimates shown in Figure S10.

We test another model (Model T2) using GPS data from only 50 GPS sites. The GPS site selection procedure is the same as that for model T1. The site distribution is shown in Figure S11, along with the spatial distribution of the smoothing distance σ_k. The optimal smoothing distance σ_0 for uncertainty estimates is 43 km. Figure S11 demonstrates that σ_k ranges 20–30 km for most of the areas involved with faults and active tectonic deformation. This is in sharp contrast with that of Model A, which shows 2–10 km smoothing distance in the same areas. The GPS-InSAR combined solution is shown in Figure 10, and Figure S12 plots the residual velocities between GPS interpolated velocities and the GPS-InSAR combined solution velocities. The result again shows significant residual velocities for the vertical component, due to dominant constraints from InSAR. The residual velocities for the horizontal component, however, are much larger than that shown in Model T1. Horizontal velocity residuals on

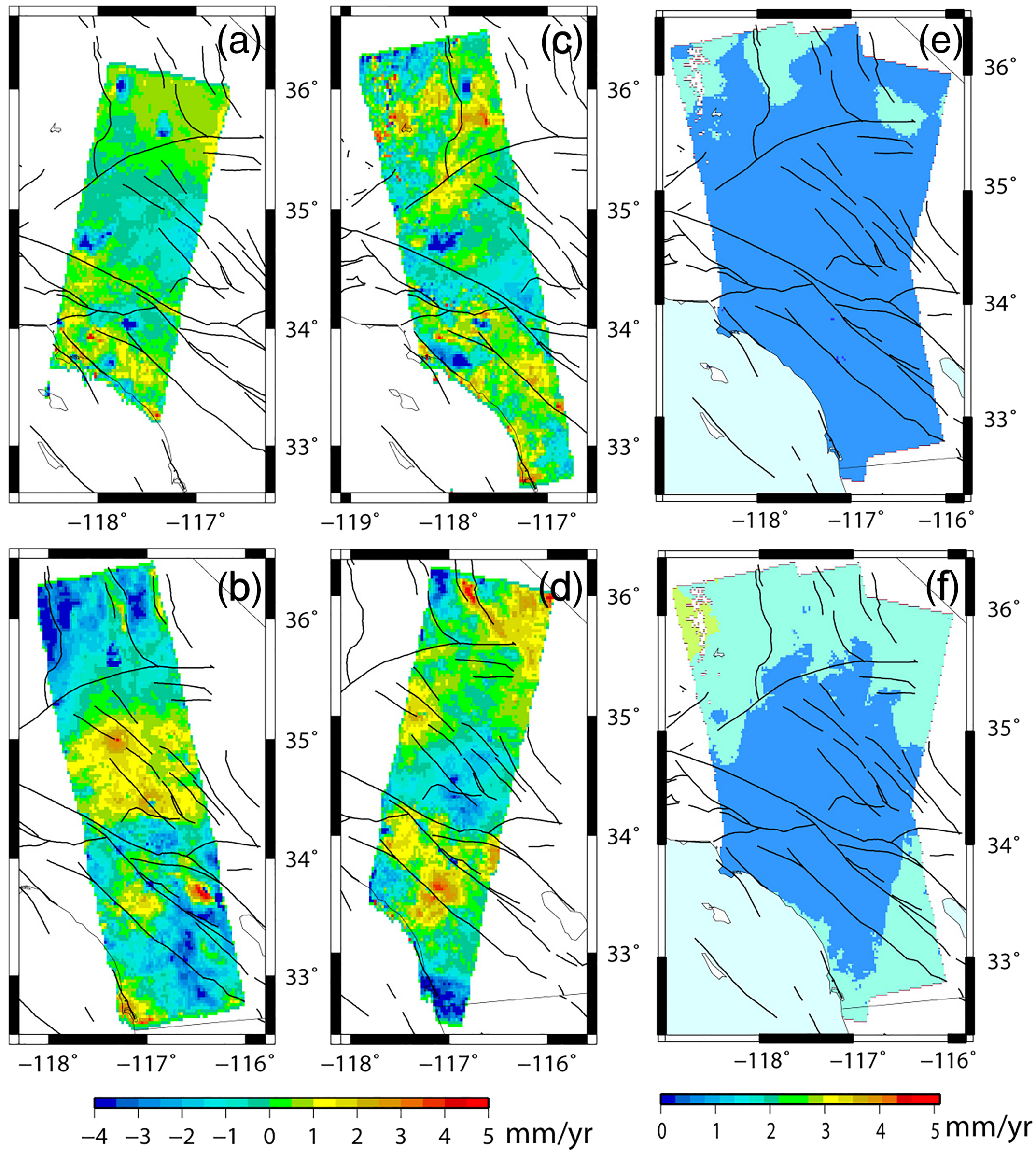

Figure 7. Data postfit residuals and solution uncertainties for model C. (a), (b), (c), and (d) are InSAR LOS postfit residuals for tracks D170, A349, A120, and D399, respectively. (e) and (f) are solution uncertainties for the east and vertical components respectively.

the order of 0.5–1.5 mm/yr are scattered over the areas imprinted with multiple tracks of InSAR data. The largest residual of ~2.5 mm/yr is spotted along the San Bernardino section of the San Andreas fault. This result suggests that for a GPS network of ~70 km spacing, incorporation of InSAR data in a region similar to Southern California will help constrain not only the vertical but also the horizontal deformation field, with solution improvements on the order of a couple of millimeters per year.

We make another comparison between GPS-InSAR combined solutions of Model T2 and Model A, and their differential velocities are shown in Figure 11. Greater differences in velocities are found in two kinds of regions: (a) the regions where active tectonic deformation takes place, such as in vicinity of the San Andreas and San Jacinto faults; and (b) the regions where GPS site distribution is sparse, such as in the southern Great Valley and western Mojave Desert. Horizontal velocity gradient of Model T2 across the San Andreas fault is less sharp as that of Model A (i.e. Figure 10 vs. Figure 4), due to relatively

10.1029/2019EA001036

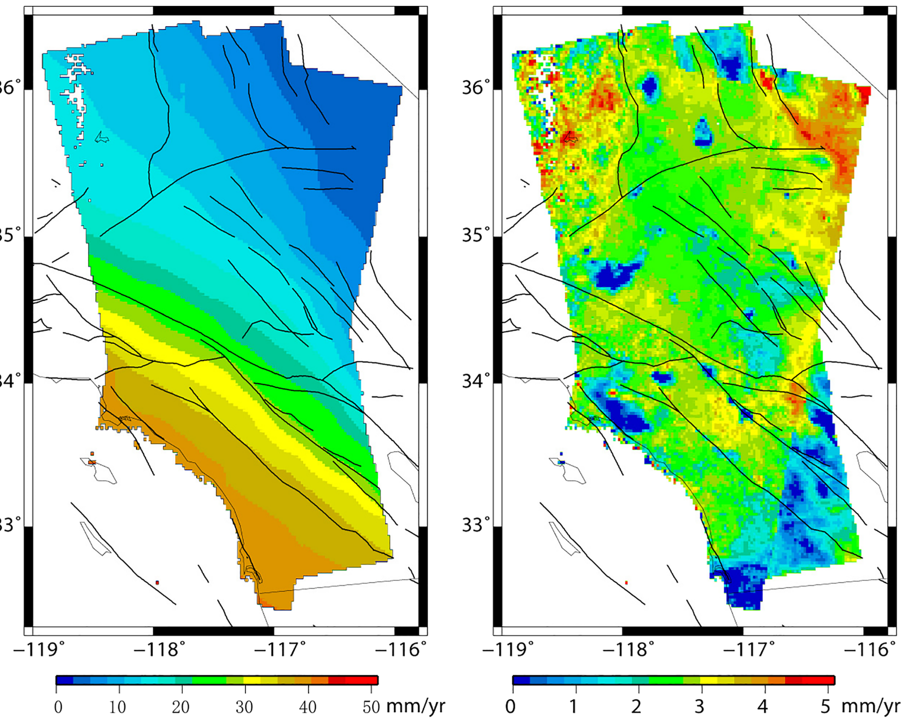

Figure 8. Velocity solution for model T1 with GPS data input of 300 sites. Left panel: Horizontal component; right panel: Vertical component.

heavier smoothing of the GPS velocity field in Model T2. The differential velocities are 0.5–2.5 mm/yr for the horizontal and 1–4 mm/yr for the vertical components for most of the areas (Figure 11), consistent with the uncertainty estimates of 0.5–1.7 mm/yr for the horizontal and 1–3 mm/yr for the vertical

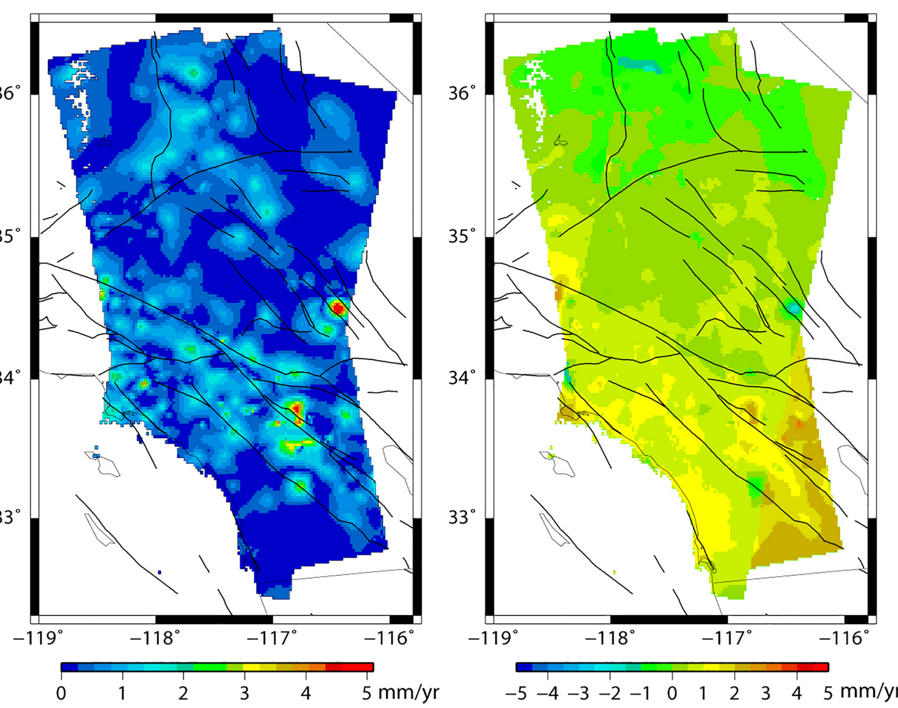

Figure 9. Velocity solution difference between model A and model T1. Left and right panels are for horizontal and vertical components, respectively.

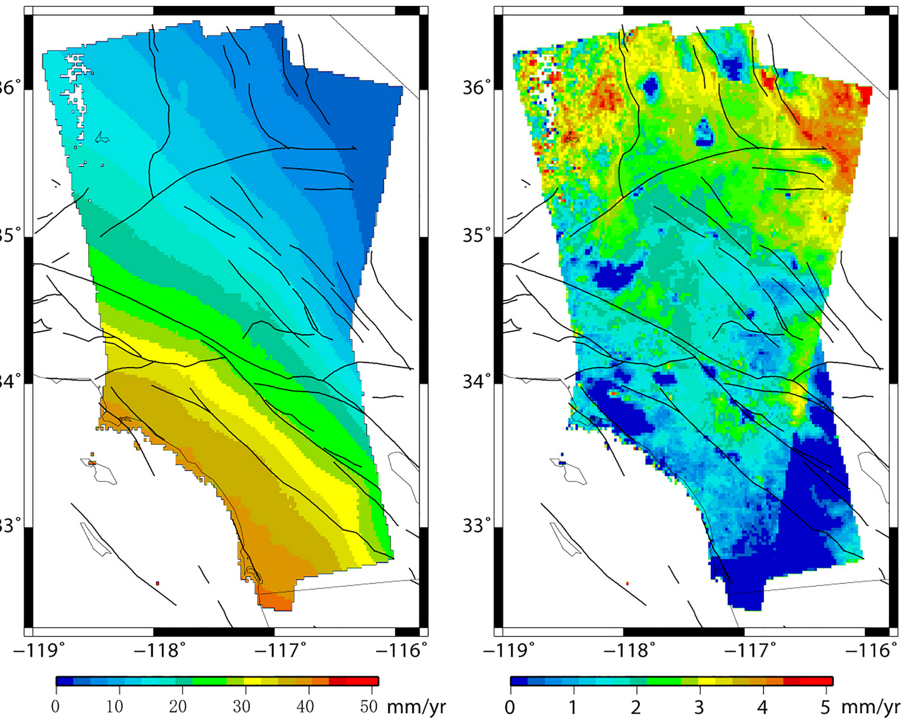

Figure 10. Velocity solution of model T2. Left panel: Horizontal component; right panel: Vertical component.

component as shown in Figure S13. Vertical velocity difference of up to 5 mm/yr is found at the southern end of the studied region for Model T2 (Figure 11), resulted from less constrained orbital ramps by GPS for the solution.

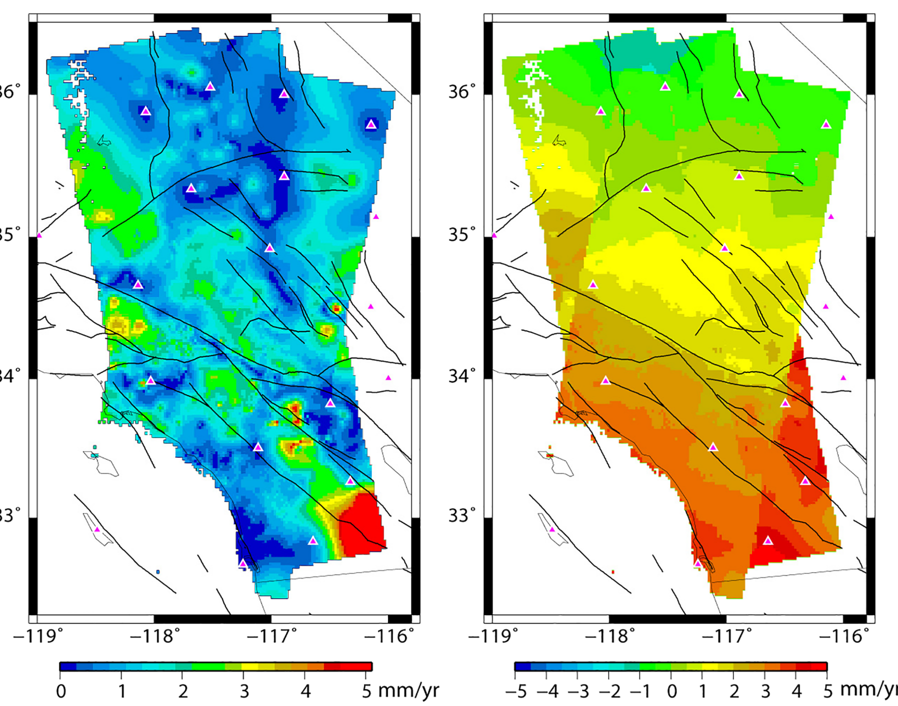

Figure 11. Velocity solution difference between model a and model T2. Left and right panels are for horizontal and vertical components, respectively.

3.3. Deformation Result Discussion

In this study we explored four models (Models A-D) of GPS-InSAR data combination for southern California using the full dataset and with different options of model constraints. Considerations of such constraints include (a) whether to estimate the ramps of satellite orbits, (b) whether to use default or estimated uncertainties to condition the InSAR data, and (c) whether to use GPS vertical velocities to constrain the final solution of vertical velocity field. Comparing all the solutions, we find that the GPS-InSAR combined horizontal velocity fields of the four models are very similar to the GPS interpolated horizontal velocity field, and the differences are at the sub-millimeter per year level for all the data points. The results suggest that the horizontal velocity solution is mostly resolved by the GPS data, and contribution from the InSAR data is relatively minor. Consistency of all the model results also suggests that InSAR and GPS observations are in good agreement in documenting the horizontal deformation field, with both velocity solutions deduced using data of overlapped time span of 6–20 years.

The difference in model constraints and/or parameterization, however, can have significant impact on vertical velocity solution and its error assessment. One of the factors involved in the combination is whether to use the GPS vertical data to constrain the pixel solution. Figures 4 and 6 show the velocity solutions of Models A and C, for which all the parameterizations are the same except that Model C incorporated GPS vertical data to constrain the model and Model A did not. Comparison of the two solutions reveals that, although inclusion of the GPS vertical data has provided additional constraints to the solution, its lack of detailed spatial resolution smeared and missed some regional deformation signals. For example, up to 8 mm/a subsidence is shown in the Lancaster, Los Angeles basin, and San Gabriel basin regions in the solutions without using GPS vertical data as constraints (Model A, Figure 4), which are however absent or significantly suppressed in the solutions using GPS vertical data constraints (Model C, Figure 6). These signals, detected by InSAR observations are caused by ground water withdrawal and shallow aquifer compaction (e.g., Galloway et al., 1998; Hoffmann et al., 2003) and are real, but cannot be picked up by GPS due to limited network spatial coverage (or missed time window).

The GPS data, on the other hand, provide effective constraints for mid to long range vertical deformation (>100 km in scale), associated with earthquake cycle and tectonic deformation. This is evidenced by the vertical deformation pattern shown in Figure 2, which is similar to that reported by Howell et al. (2016). We therefore use GPS vertical data to correct for the offsets/ramps of the InSAR data and to stabilize the long range deformation, but not to use that to constrain the local deformation.

Two sets of InSAR LOS data errors are adopted to constrain the solution in this study. One set of solutions assumes a uniform data error of 2 mm/yr (Model B), which is a common practice when no detailed error analysis is available. Another set of solutions takes the estimated uncertainties derived using the Jackknife variance estimation approach and rescaled using GPS data as reference (Models A, C, and D). Using the estimated uncertainties to weight the InSAR data, the result shows no noticeable difference from the one assuming uniform InSAR data uncertainty (e.g. Figure 4 vs. Figure S4). However, solution uncertainties hence derived for the two kinds of models are quite different. The models assuming uniform LOS rate error deduce the uncertainty estimates with a spatial pattern dictated mostly by InSAR data coverage, i.e. the redundancy distribution of the observations (e.g. Figure S5f). The models using the estimated LOS rate error yield the uncertainty estimates which take into account of the InSAR data quality and observation history, and reflect better the true data strength and weakness. For example, the solution uncertainty estimates shown in Figure 5(f) illuminate not only the impact of InSAR data redundancy, but also the strength of data input. For example, the largest uncertainties of up to 5 mm/yr are revealed at the northern and southern ends of the studied region, resulted from weak data entry of track 349.

We test different ways to remove the orbital effect from the InSAR data, and examine how that affect the data fitting of the model. Two model parameterizations are tested, one is to solve for an offset (i.e. Model D), and another is to solve for a ramp and an offset (i.e. Models A, B and C) for each of the InSAR data images respectively. The results show that by adding two free parameters for each track of the InSAR data, the orbital ramp model is able to reduce the data postfit residual chisquares by half with respect to the orbital offset model (see statistics in Table 1), attesting the necessity of ramp correction in a joint inversion involving multiple InSAR data entries. Significant jumps can also be seen for vertical solution across some of the InSAR data boundaries for Model D that adopted offset correction only (Figure S6), which however are much reduced for the vertical solutions of other models that adopted ramp corrections (Models A, B, and C, Figures 4, S4, and 6). For the data postfit residual plots, Model D shows significant jumps at the edges of image overlap (Figure S7), which however are much suppressed for other models adopted ramp removal (Figures 5, S5, and 7).

3.4. Result Interpretations

Based on the above discussion, we think that Model A takes the most optimal approach, and its result is therefore the basis for our following interpretation (Figure 4).

For the region in southern California under investigation, the horizontal velocity solution is mostly determined by GPS data, with the formal uncertainties below 0.7 mm/yr for most of the area (Figure 5). The highest velocity gradient appears across the San Andreas and San Jacinto fault system, consistent with previous findings about the deformation pattern in southern California (e.g. Tong et al., 2013; Wdowinski et al., 2007; Zeng & Shen, 2017). The formal uncertainties for the vertical component are mostly determined by InSAR data, with <1.5 mm/yr uncertainties for most of the region with more than one LOS data entry, and < 2.5 mm/yr for most of the regions with only one LOS data entry (Figure 5). Significant exceptions are for the regions in Death Valley in the northern end of the study region and near the California-Mexico border in the southern end of the study region, where the formal uncertainties are up to 5 mm/yr. This is due to relatively short duration and fewer observations for the A349 track of InSAR data. Close to zero residuals usually appear at edges of the study region, where only data from a single InSAR LOS image are available, and the solution uncertainties are relatively larger.

Local subsidence is found at several locations in southern California, such as the Los Angeles basin, Lancaster area in western Mojave, Coso geotherm site, Searles Lake, San Gabriel basin, Death Valley, Palm Springs, and area spanning the southern sections of the San Jacinto and Elsinore faults (Figure 4). The subsidence ranges 3–8 mm/yr, and possibly caused by the loss of ground water or contraction of geothermal/volcanic activity. Most of these subsidence features are recorded by more than one SAR images, and reliable. About 1–2 mm/yr subsidence appears across the southern plate boundary fault system including the San Andreas, San Jacinto, and Elsinore faults, which is slightly higher than most of the GPS observed vertical velocities. The result is mainly derived from the southeast edge of the image of track A349, and suffers from relatively larger uncertainties (~3–5 mm/yr, Figure 5(f)). More SAR data coverage in the region is needed to further confirm the feature of deformation.

Scattered uplift of about 1–3 mm/yr appears in southern Great Valley (Figure 4), and may be due to hydrologic effect associated with drought and crust rebound of the region (Amos et al., 2014). The solution uncertainties however are ~2–3 mm/yr and impede further interpretations. Uplift of about 1–3 mm/yr is also found from the northern San Jacinto Mountains across the Banning and Northern San Andreas faults to southern Mojave Desert. The result is in general consistent with the GPS vertical measurements and seems to be credible, with the solution uncertainties about 1 mm/yr (Figure 2). The area around the east end of the Garlock fault shows 2–4 mm/yr uplift, which however is not consistent with the GPS vertical velocities in the region. This deformation pattern is solved with InSAR data from the descending track 399 only, with the solution uncertainties of ~2 mm/yr. Input of more InSAR data from this area will help resolve deformation pattern of the region.

4. Conclusions

We devise an algorithm to optimally combine GPS and InSAR data and produce 3-dimensional velocity field at Earth's surface. At the locations where both InSAR and interpolated GPS data are available, optimal 3-dimensional velocity components are derived using a weighted least-square method. Both GPS and InSAR data uncertainties are used to weight the observables in joint inversion. A GPS-InSAR combination code is provided for public use. This algorithm is applied to modeling deformation field at a selected region in southern California. Conclusions are the following.

1. Using optimally estimated GPS and InSAR uncertainties to weight the data provides proper accounting of the solution uncertainties, and helps adequately assess the solution quality and reliability.
2. Including InSAR data from both ascending and descending viewing geometry, if available, provides improved constraint on the 3-D deformation when integrating with GPS data.

3. The approach of using GPS vertical data to constrain deformation field should be subject to evaluation of data quality and deformation pattern. In southern California, the current GPS network is still too sparse to adequately detect localized vertical deformation, particularly in regions affected by hydrologic processes. Existence of certain outliers in the dataset makes identification of localized deformation even more challenging. The optimal approach is therefore to use the GPS vertical data to constrain the satellite orbital ramps only, and leave the localized vertical deformation solved by InSAR, aided by GPS horizontal constraints.
4. The GPS and InSAR data are generally consistent for the horizontal velocities at sub-millimeter per year level. The vertical velocity field is determined much better for the combined solution than that using GPS data only, especially for regions experiencing localized deformation. These regions include the Los Angeles basin, San Gabriel basin, Lancaster, Palm Springs, Searles Lake, and Death Valley, where hydrologic processes caused induced subsidence of up to 3–8 mm/yr. They also include the southern Great Valley region which underwent drought related uplift of 2–3 mm/yr. Uplift of 1–3 mm/yr is detected across a transect from the northern San Jacinto Mountains to southern Mojave Desert.

Data Statement

This supporting information file supplemented to this submission includes figures associated with calibration of GPS and InSAR uncertainties, and 3D combined velocity solutions and uncertainties for Models B, D, T1, and T2. It also includes two tables for the catalogs of InSAR data and their interferograms. The supporting information dataset files submitted separately to and can be accessed through the Harvard Dataverse website https://doi.org/10.7910/DVN/QQFSQB. The file includes a sample run of the software to combine the GPS and InSAR data for a 3-D velocity solution. The GPS velocity data are from a combination of the solutions from the continuous GPS network from the MEaSUREs project (ftp://sopac-ftp.ucsd.edu/pub/timeseries/measures/ats/WesternNorthAmerica/) (Bock & Webb, 2012) and the campaign GPS network from the CMM4 project (Shen et al., 2011). The InSAR data are the LOS rate estimates of 4 tracks of ERS/Envisat measurements, averaged at 0.02 x 0.02 degree grids. The solution is for model A, with the following parameterization: (a) the estimated LOS rate data uncertainties are used for InSAR data weighting, (b) both the offsets and ramps are estimated for SAR satellite orbital errors, and (c) the GPS vertical data are not used to constrain the final pixel by pixel solution.

Acknowledgments

We appreciate editor Kristy Tiampo and two anonymous reviewers whose constructive comments helped us improve the manuscript significantly. We also thank ESA for its open policy for ERS and Envisat data and UNAVCO for archiving the data and orbital products (www.unavco.org). Continuous GPS displacement time series and velocity were produced by JPL and SIO's Orbit and Permanent Array Center (SOPAC) with support from NASA MEaSUREs program and available from MEaSUREs project (ftp://sopac-ftp.ucsd.edu/pub/timeseries/measures/ats/WesternNorthAmerica/). Part of the research was performed under a contract with the National Aeronautics and Space Administration at the Jet Propulsion Laboratory, California Institute of Technology. This research was supported by the Southern California Earthquake Center (Contribution No. 9994). SCEC is funded by NSF cooperative Agreement EAR-1600087 and USGS Cooperative Agreement G12AC20047. This research was also supported by a research grant from NSF (EAR-1723284).

References

Amos, C. B., Audet, P., Hammond, W. C., Bürgmann, R., Johanson, I. A., & Blewitt, G. (2014). Uplift and seismicity driven by groundwater depletion in Central California. *Nature*, *509*(7501), 483–486. https://doi.org/10.1038/nature13275

Bock, Y., & Melgar, D. (2016). Physical applications of GPS geodesy: A review. *Reports on Progress in Physics*, *79*(10), 106,801.

Bock, Y., & Webb, F. H. (2012). *MEaSUREs Solid Earth Science ESDR System*. La Jolla,California and Pasadena, California USA: Digital media.

Efron, B., & Stein, C. (1981). The Jackknife estimate of variance. *Ann. Statist.*, *9*(3), 586–596. https://doi.org/10.1214/aos/1176345462

Fattahi, H., & Amelung, F. (2014). InSAR uncertainty due to orbital errors. *Geophysical Journal International*, *199*(1), 549–560. https://doi.org/10.1093/gji/ggu276

Galloway, D. L., Hudnut, K. W., Ingebritsen, S. E., Phillips, S. P., Peltzer, G., Rogez, F., & Rosen, P. A. (1998). Detection of aquifer system compaction and land subsidence using interferometric synthetic aperture radar, Antelope Valley, Mojave Desert, California. *Water Resources Research*, *34*(10), 2573–2585.

Gens, R., & Van Genderen, J. L. (1996). Review article SAR interferometry—Issues, techniques, applications. *International Journal of Remote Sensing*, *17*(10), 1803–1835.

Gudmundsson, S., Sigmundsson, F., & Carstensen, J. M. (2002). Three-dimensional surface motion maps estimated from combined interferometric synthetic aperture radar and GPS data. *Journal of Geophysical Research*, *107*(B10), 2250. https://doi.org/10.1029/2001JB000283

Herring, T., Craymer, M., Sella, G., Snay, R., Blewitt, G., Bock, Y., et al. (2008). SNARF 2.0: a regional reference frame for North America. In *AGU Spring Meeting Abstracts*.

Hoffmann, J., Galloway, D. L., & Zebker, H. A. (2003). Inverse modeling of interbed storage parameters using land subsidence observations, Antelope Valley, California. *Water Resources Research*, *39*(2), 1031. https://doi.org/10.1029/2001WR001252

Howell, S., Smith-Konter, B., Frazer, N., Tong, X., & Sandwell, D. (2016). The vertical fingerprint of earthquake cycle loading in southern California. *Nature Geoscience*, *9*(8), 611–614.

Liu, Z., Lundgren, P., Shen, Z. (2014). Improved imaging of Southern California crustal deformation using InSAR and GPS, *SCEC Annual Meeting*, SCEC contribution# 2038.

Marinkovic, P., Larsen, Y. (2013). Consequences of Long-Term ASAR Local Oscillator Frequency Decay - an Empirical Study of 10 Years of Data, *ESA Living Planet Symposium*, Edinburgh, UK.

Samsonov, S. (2010). Topographic correction for ALOS PALSAR interferometry. *IEEE Transactions on Geoscience and Remote Sensing*, *48*(7), 3020–3027.

Samsonov, S., Tiampo, K., Rundle, J., & Li, Z. (2007). Application of DInSAR-GPS optimization for derivation of fine-scale surface motion maps of Southern California. *IEEE Transactions on Geoscience and Remote Sensing*, *45*(2), 512–521.

Samsonov, S. V., Tiampo, K. F., & Rundle, J. B. (2008). Application of DInSAR-GPS optimization for derivation of three-dimensional surface motion of the southern California region along the San Andreas fault. *Computers & Geosciences*, *34*(5), 503–514.

Sansosti, E., Casu, F., Manzo, M., & Lanari, R. (2010). Space-borne radar interferometry techniques for the generation of deformation time series: An advanced tool for Earth's surface displacement analysis. *Geophysical Research Letters*, *37*, L20305. https://doi.org/10.1029/2010GL044379

Shen, Z.-K., King, R., Agnew, D., Wang, M., Herring, T. A., Dong, D., & Fang, P. (2011). A unified analysis of crustal motion in Southern California, 1970-2004: The SCEC crustal motion map. *Journal of Geophysical Research*, *116*, B11402. https://doi.org/10.1029/2011JB008549

Shen, Z. K., Wang, M., Zeng, Y., & Wang, F. (2015). Strain determination using spatially discrete geodetic data. *Bulletin of the Seismological Society of America*, *105*(4), 2117–2127. https://doi.org/10.1785/0120140247

Tong, X., Sandwell, D. T., & Smith-Konter, B. R. (2013). High-resolution interseismic velocity data along the San Andreas Fault from GPS and InSAR. *Journal of Geophysical Research - Solid Earth*, *118*, 369–389. https://doi.org/10.1029/2012JB009442

Wdowinski, S., Smith-Konter, B., Bock, Y., & Sandwell, D. (2007). Diffuse interseismic deformation across the Pacific–North America plate boundary. *Geology*, *35*(4), 311–314.

Zeng, Y., & Shen, Z. K. (2017). A fault-based model for crustal deformation in the Western United States based on a combined inversion of GPS and geologic InputsA fault-based model for crustal deformation in the WUS based on a combined inversion of GPS. *Bulletin of the Seismological Society of America*, *107*(6), 2597–2612.